

Archie's exponents in complex lithologies derived from 3D digital core analysis

M.A. Knackstedt, C. H. Arns, A.P. Sheppard, T. J. Senden and R. M. Sok, Australian National University, Y. Cinar and W. V. Pinczewski, University of New South Wales, M. Ioannidis and G. S. Padhy, University of Waterloo.

Copyright 2007, held jointly by the Society of Petrophysicists and Well Log Analysts (SPWLA) and the submitting authors.

This paper was prepared for presentation at the SPWLA 48th Annual Logging Symposium held in Austin, Texas, United States, June 3-6, 2007.

ABSTRACT

The values of Archie's exponents (m and n) play a significant role in formation evaluation. Conventionally, values are assumed to be $m = n = 2$. Significant scatter in laboratory measured data for m and n have been noted and this is usually attributed to rock heterogeneity, the complicated pore structure in complex lithologies and wettability characteristics at the pore scale. Attempts to provide an understanding for observed resistivity behavior primarily refer to ideal systems (e.g., sintered glass bead packs) which do not exhibit the complexity of reservoir core. 3D imaging and analysis of the pore scale structure within core material allows one to directly measure the pore structure, tortuosity and degree of interconnections of the pore systems and the spatial distribution of the fluid phases. This can give insight into the behavior of m and n in realistic pore geometries.

This paper presents the results of a 3D pore scale study of the relationship between Archie's m and n values and pore structure in 12 model and reservoir core samples. The samples are imaged in 3D across a range of length scales down to 2.5 microns resolution. Samples include sintered bead packs, homogeneous unconsolidated and consolidated sandstones, thinly bedded samples, sucrosic dolomites, dual porosity samples and heterogeneous carbonate reservoir core. Resistivity as a function of saturation is directly calculated on the image data and the effective m and n determined. Where available, the 3D pore scale data is compared with experimental data obtained on the same or sister core material with reasonable agreement.

Variations from conventional values of m and n are noted. The cementation exponent m exhibits a small dependence on porosity for clastic and homogeneous carbonate samples and varies with the proportion of disconnected porosity in vuggy carbonate systems. The saturation exponent n often exhibits a dependence on saturation. Analysis on a thinly bedded sand shows strong anisotropy in val-

ues with orientation. Carbonate cores, which include a significant proportion of microporosity exhibit low values of n . In all cases wettability has a strong effect on the saturation exponent. We consider the relative interconnectivity and tortuosity of pores and fluid phases in the different samples and their contribution to the electrical transport. This pore scale quantification possible from micro-CT imaging can aid in explaining the observed values of m and n for reservoir core material.

INTRODUCTION

Archie's equations form the basis of resistivity log interpretation. They are written as:

$$F = \frac{R_0}{R_w} = \frac{a}{\phi^m} \quad (1)$$

and

$$RI = \frac{R_t}{R_0} = S_w^{-n}. \quad (2)$$

The formation factor F is defined as the ratio of the brine saturated rock resistivity R_0 to the resistivity of the brine R_w . The resistivity index RI is the ratio of the resistivity of the partially brine-saturated rock R_t to R_0 . m and n are the cementation and saturation exponents and a is an empirical constant.

The empirical relationships in Eqns. 1-2 are applicable to a wide variety of rock types. In general the cementation exponent m increases as the rock becomes more consolidated and more cemented. (Carothers, 1968) reported variations in m from 1.5 for unconsolidated sands to 2.2 for more compacted sands. Carbonates may exhibit a wider variation in m . (Focke and Munn, 1987) observed m values from 2.0 for grainstones and sucrosic dolomites to $m > 5.0$ for poorly interconnected (vuggy) cores.

The evaluation of n in partially saturated rocks is even more complicated. In this case the pore geometry and the relative locations of the fluid phases influences the empirical exponent. Wettability in particular has a dramatic effect on the resistivity response of partially saturated rocks. (Sharma et al., 1990; Sweeney and Jennings,

Table 1: Archie vs. non-Archie conditions (Worthington, 2005)

Archie Conditions	Non-Archie Conditions
Single Rock Type	Multiple Rock Type
Homogeneous	Heterogeneous
Isotropic	Anisotropic
Single Pore Size	Multimodal Pore Size
Compositionally Clean	Clay minerals
Intergranular Porosity	Intragranular/Microporosity
Water Wet	Mixed/Oil Wet
$S_w > 15\%$	$S_w < 15\%$

1960) report variations in n from $n < 2$ to $n > 6$ under different wettability conditions on the same core material.

The observed scatter in n is further complicated by violations to the assumption of standard Archie rock behaviour. For the purposes of petrophysical evaluation, in classical Archie reservoir rocks it is assumed that the saturation exponent n is constant for a given (clean) sample of rock. This presumed constancy forms the basis for the determination of water saturation from RI measurement on a particular rock. It has been shown that many rocks exhibit changes in n with variations in S_w for the same rock (Worthington and Pallatt, 1992; Fleury et al., 2004). The nature of this dependence has important implications to the evaluation of oil-in-place. (Worthington, 2005) discussed the strict conditions under which rocks could be classified as Archie rocks (see Table 1); non Archie rocks infringe upon one or more of these conditions.

Attempts to provide a theoretical understanding for observed resistivity behavior primarily refer to ideal systems (e.g., sintered glass bead packs) which do not reflect the complex conditions listed in Table 1. 3D imaging and analysis of reservoir core material allows one to directly measure the pore structure, tortuosity and degree of interconnections of the pore systems and the distribution of the fluid phases under different wettability conditions. This allows one to potentially probe the role of deviations from strict Archie conditions on the behaviour of m and n and may give insight into the behavior of m and n in complex pore systems. In previous work we have described the development of a capacity to characterize and numerically predict petrophysical properties from experimental 3D microtomographic images of rock microstructures (Arns et al., 2005b). Transport properties derived from image data and computational analysis of a range of cores including reservoir sands and carbonates have been compared with conventional laboratory measurements and shown to be in good agreement (Arns et

al., 2001; Arns et al., 2004; Knackstedt et al., 2004; Arns et al., 2005a).

In this paper we present the results of a 3D pore scale study of the relationship between Archie's m and n values and pore structure in a set of 12 model and reservoir core samples. Rock samples are imaged in 3D across a range of length scales down to 2 microns resolution. Samples include sintered bead packs, homogeneous unconsolidated and consolidated sandstones, thinly bedded samples, sucrosic dolomites, dual porosity samples and heterogeneous carbonate reservoir core. Resistivity as a function of saturation is directly calculated on the image data and the effective m and n measured. Where available the 3D pore scale data is compared with experimental data obtained on the same or sister core material.

We first describe results for a set of samples which exhibit Archie characteristics (Single rock type, homogeneous, isotropic, clean, dominant pore size and water wet). We find that Archie's cementation exponent varies with porosity in agreement with experiments performed on sister core material. The resistivity exponent is constant for most samples down to lower saturations; deviations in n may occur for $\phi > 15\%$. We then investigate the role of wettability on the saturation exponent; strong differences in n are noted for different wettability scenarios. The relative interconnectivity of the water filled pore space can be directly measured on the 3D image data. This fluid distribution is systematically related to the resultant behaviour of n . We then illustrate the effect of anisotropy on the Archie's exponents; estimates of n in thinly laminated sands exhibit strong dependence on orientation. A complex sample exhibiting dual pore sizes behaves like an Archie rock and exhibits conventional values of m and saturation dependence on n in spite of the multimodal pore size distribution. Finally a set of heterogeneous carbonate cores with multiple pore sizes are studied. For these systems the exponent n is quite low and found to vary strongly with saturation. Microporosity is shown to have a dramatic effect on the behaviour of Archie's exponents. In all cases the quantification of the pore geometry and fluid saturation distributions in 3D aids in the interpretation of the resistivity behaviour. Results of the study demonstrate the feasibility of combining 3D digitized images with numerical calculations to predict the resistivity of core material.

METHODS AND SAMPLES

This section describes the methodology of image acquisition and phase identification methods for the samples studied.

Table 2: Samples considered in this study and sample details. Porosity based on the image data is given. Experimental porosity is within $\pm 1\%$ for all homogeneous samples and $\pm 3\%$ for all heterogeneous samples. Sample size (Size) is given in mm and voxel size or resolution (Res.) is given in microns. In the cases starred (*) the experimental porosity is measured on a sister plug and not on the imaged sample; direct comparison is therefore subject to larger errors.

	Sample Type	ϕ_{im}	ϕ_{exp}	Size	Res.
	Archie Rocks				
1	Bead Pack	38.3%	39.1%	55	30
2	Fontainebleau1	17.8%	17.4%	5	2.85
3	Fontainebleau2	13.2%	13.1%	5	2.85
4	Fontainebleau3	6.8%	7.7%	5	2.85
5	Suc. DoloA	28.3%	27.9%	5	2.85
6	Suc. DoloB	19.5%	19.1%	5	2.85
7	Suc. DoloC	18.1%	18.6%	5	2.85
8	Suc. DoloD	12.0%	12.8%	5	2.85
9	Anisotropic Aeolian Sand	18.4%	21%*	8	4.2
10	Dual-scale Model 1	54.7%	46.8%*	9	5.0
	Multi-Scale				
11	Bioclastic 1	27.1%	28.9%	5.0	2.8
12	Bioclastic 2	23.2%	26.7%	5.0	2.8

Tomographic Imaging

A high-resolution and large-field X-ray μ CT facility has been used to analyse the 3D structure in core plugs across a range of scales down to 2.5 microns. All images are composed of 2048^3 voxels. Details of the equipment and experimental methodology used to image the microstructure of sedimentary rock have been given previously (Sakellariou et al., 2004a; Sakellariou et al., 2004b; Arns et al., 2005b).

Samples studied and 3D Image Data

All reservoir samples were originally provided as core or plugs. Samples were cleaned and subsamples were typically cut using a 5-8 mm diameter diamond coring tool on the original core material. Image data on all samples was obtained at resolutions of 2.5-30 micron voxel size. Table 2 lists the sample type, porosity, image size and image resolution for all samples considered in this study.

Archie Rocks

Eight Archie-type rocks are chosen for this study; a monodisperse bead pack, three Fontainebleau sandstone samples and four sucrosic dolomite samples. Sample information is given in Table 2. In Fig. 1 we show exam-

ples of slices through the 3D images of these Archie-type rocks. The image quality enables one to discern the individual pore and grain structure. Mercury injection capillary pressure measurements (MICP) on these samples show that the pore space is dominated by intergranular porosity; $> 95\%$ of the pores are $\geq 3 \mu\text{m}$ in diameter. In Fig. 2(a) we show an example of the MICP data for the Sucrosic Dolomite Sample 2 (Fig. 1(d)).

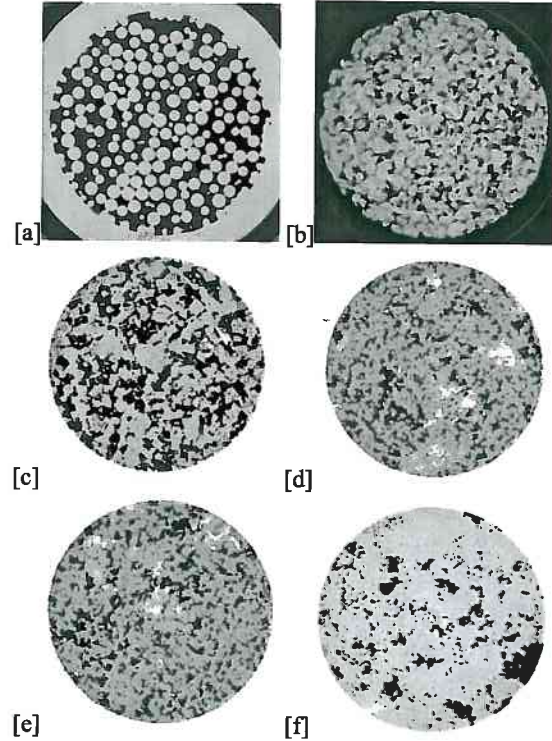


Figure 1: Grey scale tomographic images of the Archie rock subsamples. (a) bead pack, (b) Fontainebleau sandstone, (c-f) sucrosic dolomites. Image sizes and resolutions are detailed in Table 2.

Anisotropic sample

In Fig. 3 we show a slice of a clean aeolian sandstone sample. The aeolian sand exhibits fine scale laminations at the mm scale. In the image volume 6 distinct bedding planes are evident.

Dual porosity sample

In Fig. 4 we show a slice of a clean sample exhibiting dual porosity. The sample is an artificial vuggy carbonate sample. This sample is created by consolidating monodisperse glass beads ($125\text{-}150 \mu\text{m}$ diameter) and CaCO_3 particles ($1.18\text{-}2.38 \text{ mm}$) in an oven, and then dissolving the carbonate particles by flowing acid (Padhy

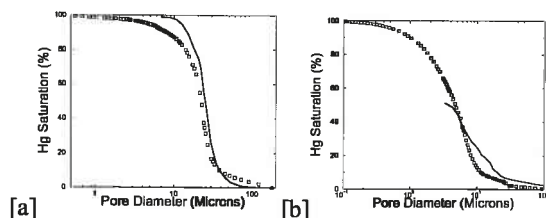


Figure 2: (a) MICP curve for sucrosic dolomite sample 2. The data points give the experimental data. The solid line is the numerical prediction of the MICP data from the image data. (b) MICP experimental data for one of the heterogeneous bioclastic grain/packstone samples. Only $\approx 50\%$ of the pore space is connected via resolvable throats in the image data. The remainder of the pore space is not resolvable via the current micro-CT instrument.

et al., 2006). The sample exhibits a high porosity inter-granular medium decorated with large vugs.

Bioclastic Grain/Packstone

Two heterogeneous carbonate samples from one of the main oil producing reservoirs in Abu Dhabi, UAE are considered (Sok et al., 2007). They are totally composed of carbonates of the Lower Cretaceous age, deposited

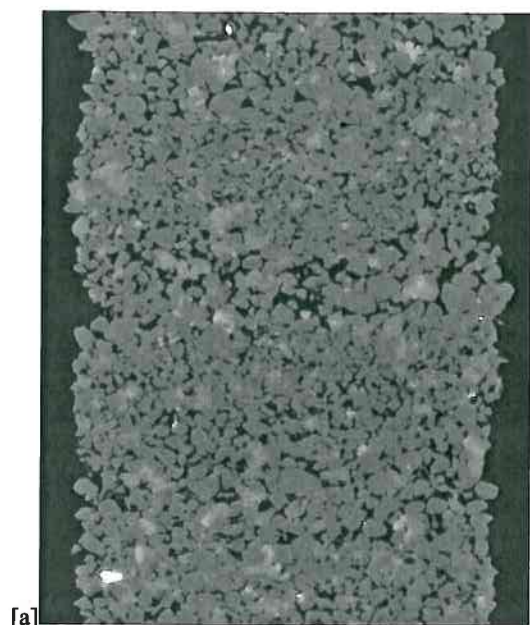


Figure 3: Grey scale tomographic images of the clean laminated aeolian sand. Image sizes are detailed in Table 2.

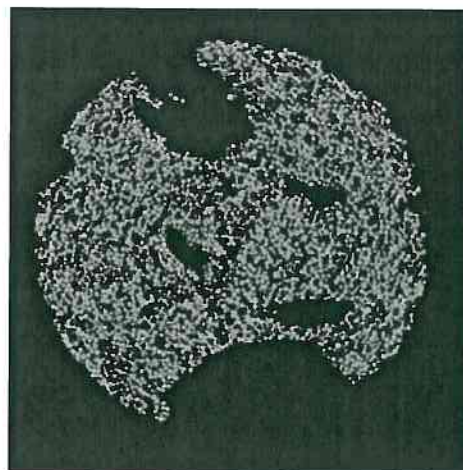


Figure 4: Grey scale tomographic images of the artificial vuggy (dual porosity) carbonate sample. Image sizes are detailed in Table 2.

in a shallow shelf environment. The core is composed mainly of bioclastic grainstone and packstone with some algal fragments which form vuggy pore spaces. Examples of orthogonal 2D slices through the tomographic data are shown in Fig. 5. From MICP experiments on the samples we note that $\approx 50\%$ of the porosity is accessible via throats of diameter ≤ 3 microns (see Fig. 2(b)). One would therefore expect a significant proportion of unresolvable porosity (microporosity) in the image data.

Phase Identification

In this subsection we review the methods used to identify the pore phase in the image volumes. First we describe the method used on most samples which allow good differentiation between the pore and mineral phases (samples 1-10). We then describe the methodology used for samples with significant proportions of microporosity (samples 11-12).

Homogeneous with majority resolvable porosity

The tomographic image consists of a cubic array of reconstructed linear x-ray attenuation coefficient values, each corresponding to a finite volume cube (voxel) of the sample. Ideally one would wish to have a multi-modal attenuation distribution giving unambiguous phase separation of the pore phase from mineral phase peaks. This idealized phase extraction is possible on the samples 1-10. Comparison of image porosity to experimentally measured porosity on the imaged sample is given in Table 2. The agreement is excellent for all samples.

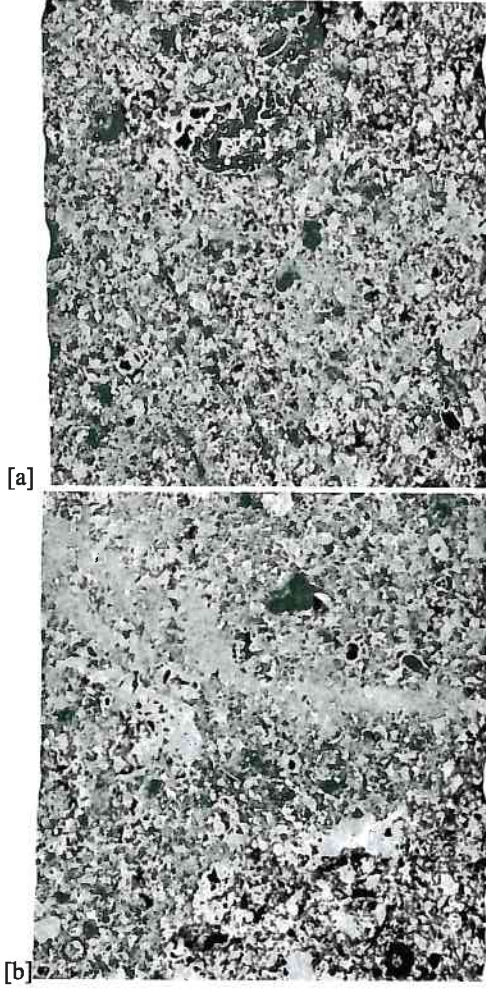


Figure 5: Grey scale tomographic images of the carbonate samples (a) 11 and (b) 12.

Microporous samples: Complex carbonates

Unfortunately in the bioclastic carbonate samples the presence of pores at scales below the image resolution (measured via MICP) leads to a broad spread in the low density signal making it difficult to *unambiguously* differentiate the pore from the microporous and solid mineral phases. The methods used to identify porosity in these heterogeneous systems has been described in more detail elsewhere (Sok et al., 2007). Here we briefly describe the method for the bioclastic sample in Fig. 5(a).

The intensity histograms for the sample is given in Fig. 6; a pore and solid peak are discernible, with an extensive intermediate attenuation range. Porosity associated with the resolved pore phase is 17% while the total porosity of the samples is experimentally measured (He/Hg) at 28.9%. The intermediate attenuation region is associated

Table 3: Carbonate porosity: Experimental ϕ_{exp} , Resolvable image porosity $\phi_{image,res}$, resolved and connected image porosity $\phi_{connect}$ and image porosity including microporous contribution $\phi_{image,tot}$. Details of the method and results are given in (Sok et al., 2007).

Sample	ϕ_{exp}	$\phi_{image,res}$	$\phi_{connect}$	$\phi_{image,tot}$
11	28.9%	17.0%	8.8%	27.1%
12	26.7%	10.8%	1.7%	23.2%

with pores below image resolution; the meso/microporous phase. Phase separation is performed on the image data to include porosity contributions from the microporous phase (Sok et al., 2007).

Mean attenuation values for the phases (\bar{I}_{phase}) and their standard deviation (σ_{phase}) are determined from the histogram. Porosities within the intermediate phase are assigned by analysing the individual voxel intensities within that phase. To any voxel n in the intermediate phase that has an intensity value $I_n < \bar{I}_{pore} + \sigma_{pore}$ we assign 100% microporosity. To any voxel in the intermediate phase with $I_n \geq \bar{I}_{solid} - \sigma_{solid}$ we assign 0% microporosity. Any voxel with I_n in between these two cut-off intensities, we assign a linearly scaled microporosity value $\phi_{micro,n}$:

$$\phi_{micro,n} = \frac{((\bar{I}_{solid} - \sigma_{solid}) - I_n)}{(\bar{I}_{solid} - \sigma_{solid}) - (\bar{I}_{pore} + \sigma_{pore})}, \quad (3)$$

and the total porosity ϕ is then calculated as

$$\phi = \frac{N_p + \sum_{n=0}^{N_i} \phi_{micro,n}}{N_{tot}}, \quad (4)$$

where N_p is the number of voxels in the pore phase, N_i the number of voxels in the intermediate phase, and N_{tot} is the total number of voxels in the sample. Based on this analysis the **total porosity** for sample 11 is $\phi = 27.1\%$ in reasonable agreement with the data obtained from Hg porosimetry ($\phi = 28.9\%$). Sample 12 gives $\phi = 23.2\%$, slightly underestimating the prediction obtained from Hg porosimetry ($\phi = 26.7\%$). One can also spatially identify connected macropores, macropores connected via the microporous phase, isolated macropores and microporosity within the image volume (Fig. 6 (lower)). The data is summarized in Table 3.

Image quality control: Match to MICP data

A measure of the quality of the image based data has already been directly undertaken by comparing the porosity measured on the image data to porosity measured via He/Hg porosimetry. A more rigorous test of the image data is available by comparing the experimental measurement of the pore throat size via MICP on the imaged

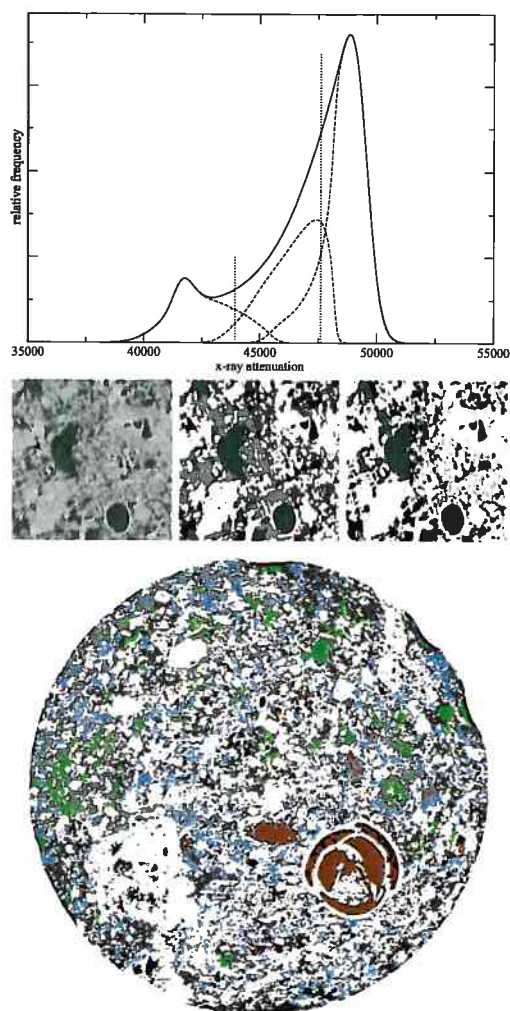


Figure 6: (Upper) Intensity histogram for bioclastic grain/packstone sample. The solid line shows the total intensity histogram, the dashed lines the (resultant) histograms of the three phases after segmentation. The dotted vertical lines show the initial thresholds (T_{pore} , T_{solid}) for the microporosity analysis. (Center) Result of three phase segmentation. The left image shows a small subset of the middle z-slice of the original dataset of sample 9. The middle image shows the resulting partitioning after the three phase segmentation. The black represents the pore-phase, the grey the intermediate phase and the white the rock phase. The right image shows the grey-level encoded microporosity analysis of the intermediate phase. (Lower) shows the composite image with different phases identified. Green gives the connected macroporous phase, red the macropore phase connected after inclusion of low density microporosity $\phi_{micro} > 75\%$, and blue the high density microporous phase $\phi_{micro} < 25\%$. The white phase is the solid, the grey the microporous phase $75\% > \phi_{micro} > 25\%$. The black phase are macropores which remain disconnected after inclusion of the meso/micropore phase (Sok et al., 2007).

core material to simulations of MICP performed directly on the images (Arns et al., 2005b).

Homogeneous samples with resolvable porosity

An example of the direct comparison of the numerically-based MICP simulation to experimental MICP data is given in Fig. 2(a) for one of the sucrosic dolomite samples. Close agreement can be seen across the range of pore sizes. This result is common for all Samples 1-10. From this we conclude that the image data is a reliable representation of the 3D pore structure of the sample.

Heterogeneous samples with microporosity

A comparison between numerical and experimental MICP data for Samples 11-12 (example shown in Fig. 2(b)) is satisfactory over the range of pore throat sizes resolved in the image data. The throat size below image resolution cannot be discerned from the image data.

CALCULATION OF RESISTIVITY FROM IMAGE DATA

A microstructure defined by a digital image is already naturally discretized and lends itself immediately to numerical computation of many properties. In this subsection we describe the numerical methods used to calculate resistivity properties (Formation factor and Resistivity Index (RI)) directly on the 3D digital images. We then describe the numerical results obtained on the imaged samples.

Methodology

We use a finite-element method (FEM) to estimate the electrical conductivity of the model system. FEM uses a variational formulation of the linear conductivity equations and solves Laplace equation by minimizing the energy using a fast conjugate-gradient method. Each voxel is taken to be a trilinear finite element. Non-periodic boundary conditions are used and calculations carried out for voltage gradients applied along each of the major tomogram axes, giving three principal conductivities defined by the tomogram axes. The FEM solver is based on previous work (Garboczi and Day, 1995; Arns et al., 2002; Bohn and Garboczi, 2003). The current version uses a block-wise decomposition of the physical domain onto $N_x \times N_y \times N_z$ processors using the MPI protocol, incorporates density maps, partitions and effective medium theories for the assignment of material properties, and scales linearly to system sizes well above 1000^3 voxel (tested for 256 processors). Symmetries within bulk materials are used to reduce the computational load. For the formation factor calculation we consider an idealized case assigning zero conductivity to the

solid phase and $\sigma_{water} = 1$ in the resolved (macroporosity). Voxels in a microporous phase are assigned the conductivity of the microporous phase via Archie's law; $\sigma_{micro} = \sigma_{water} \times \phi_{micro,n}^m$, where $m = 2$.

For the RI calculation both the non-wetting phase and the mineral phase is assumed to be non-conductive and water phase and the microporosity is considered conductive. We consider two extremes of wettability; strongly oil-wet and strongly water-wet. The fluid geometries are distributed assuming the fluids have migrated and occupy the most favourable pore spaces; for the water wet case the oil will fill the largest pores and throats while the water will preferentially occupy the smaller pores and throats. In the oil wet case the fluid distributions are reversed; oil will now preferentially occupy the smaller pores and throats. To define the phase distribution at different saturations and under varying wetting conditions we define locally on the image the diameter of the largest sphere which lies within the pore space and covers every voxel (r_{local}). Non wetting fluid resides in the regions of large covering sphere radius $R > r_{local}$ and the wetting fluid resides in regions with small covering radius $R \leq r_{local}$. By incrementing the value of the sphere radius R one can vary the effective saturation. An illustration of the fluid distributions within a small subset of an unconsolidated sample volume under water-wet conditions at high and low water saturations is shown in 2D in Fig. 7. A snapshot of pore network structure and the oil and water distributions at intermediate water saturations is shown in 3D in Fig. 8. We observe that the oil distribution is dominated by the pore morphology; the phase distribution roughly coincides with the structure of the pore space. The structure of the wetting phase at low saturations (Fig. 8(c)) becomes more complex due to the presence of wetting films in the corners of the pore space.

Different scenarios for fluid distributions are considered (Toumelin et al., 2006). Drainage of a water-wet rock model is simulated via propagation of the non-wetting phase from the the periphery of the core inwards. Invasion of oil into an oil wet sample is simulated via film thickening of the non-wetting fluid in regions of small radius (high capillary pressure) and gradual film thickening. Imbibition (water injection) into the water wet rock is also simulated via film thickening. In the samples with microporosity we assume the microporosity remains water saturated.

Archie Rocks

Formation Factor Cementation Exponent m

Simulations of resistivity under fully water saturated conditions are performed on significant subsets of the full

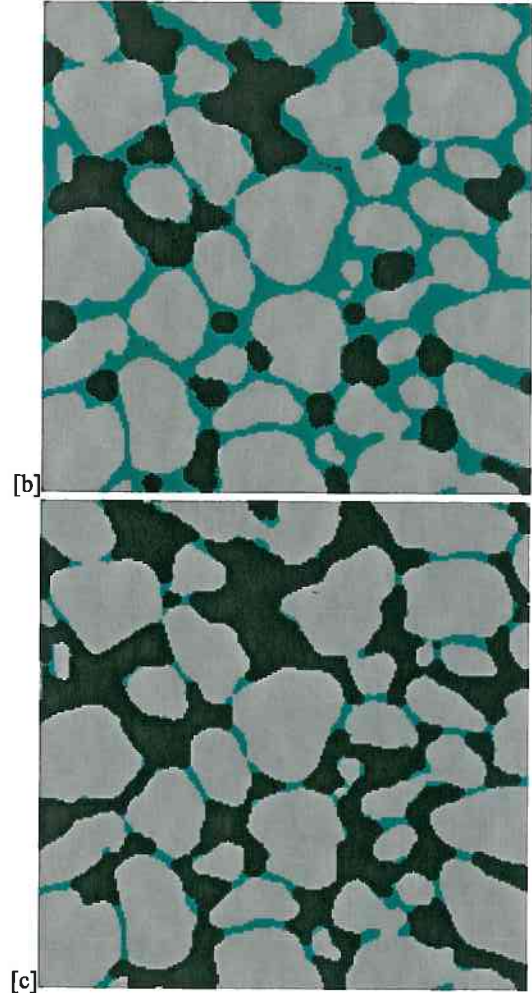


Figure 7: Illustration in 2D of wetting phase distribution (blue) within the pore space (black) of a poorly consolidated sand sample. (a) is a snapshot at higher ($\approx 55\%$) water phase saturation and (b) at low (near irreducible, $\approx 15\%$) water saturation.

image volume ($1200^3 - 1400^3$) along three orthogonal axes.

Sintered Bead Pack: The value of m derived from the image data along three orthogonal axes is $m_x = 1.42$, $m_y = 1.41$ and $m_z = 1.40$. This results in excellent agreement with experimental and model data obtained previously on sintered glass bead packs; in particular (Sharma et al., 1990) performed a number of experiments on lightly sintered glass bead packs and obtained a value of $\bar{m} = 1.39 \pm .1$. The result is also in good agreement with the work of (Wong et al., 1984) for fused glass beads.

Fontainebleau Sandstone: The data for the three Fontainebleau sandstone samples is given in Fig. 9 where we plot

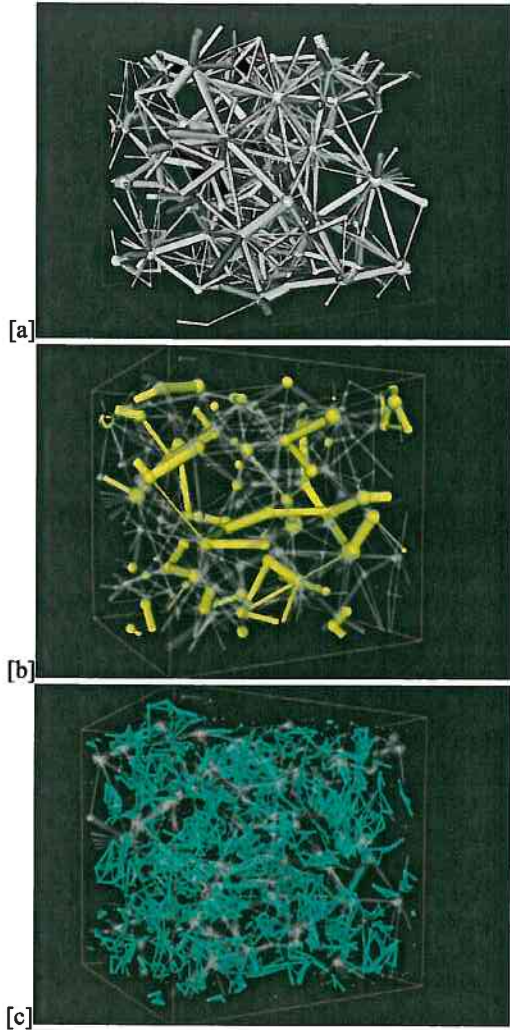


Figure 8: Illustration in 3D of wetting phase distribution within the pore space of an Ottawa sand sample. (a) shows a 3D realization of a small subset of the total pore network, (b) shows the distribution of the non-wetting phase at $S_w = 55\%$ in yellow along with the original pore network (partially transparent grey). (c) shows the distribution of the wetting phase at $S_w = 15\%$; near S_{wi} with the original pore network rendered partially transparent.

the cementation exponent m as a function of porosity ϕ . Comparison with experimental data for Fontainebleau is also shown. For the higher porosity samples we observe a consistent value of m and a significant increase in m at $\phi \simeq 7\%$. This is in agreement with experimental data wh

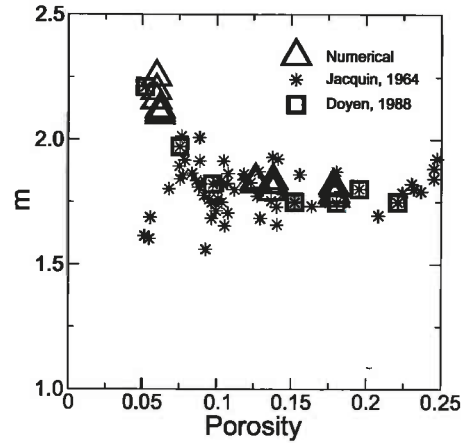


Figure 9: $m(\phi)$ vs. ϕ plot for the three Fontainebleau samples in comparison with experimental data. Experimental data from (Jacquin, 1964) and (Doyen, 1988) is shown. Simulation data on the large image volume in three orthogonal directions is given by the triangles.

Sucrosic Dolomites: Results for the cementation exponent measured along three orthogonal axes are given in Table 4. The high porosity sample exhibits a cementation exponent $m \simeq 1.8$, while Samples B and C both exhibit $m = 2$. The low porosity sample exhibits a suprisingly high value of m . No anisotropy in m is noted in the four samples. (Focke and Munn, 1987) showed extensive laboratory data for the cementation exponent of sucrosic dolomites with intercrystalline porosity and open textures; in all cases the value of m was approximately 2. Three of the four samples exhibit this classical behaviour. Sample D, which exhibits poorer connectivity gives a significantly higher value of m . Experimental measurement of m was undertaken on (larger) sister core plugs to the image data. In Fig. 10 we plot the behaviour of m vs ϕ for the image data and this experimental data. We observe reasonable agreement between the image and experimental data and in both cases observe a strong increase in m with decreasing ϕ ; particularly for $\phi < 0.175$.

Saturation Exponent n

Saturation exponents were calculated from simulation of oil injection into a water saturated pore space under two

Table 4: Resultant cementation exponent for the four sucrosic dolomite samples.

Sample	m_x	m_y	m_z
A	1.81	1.81	1.83
B	2.02	2.01	2.00
C	2.07	2.09	2.04
D	3.00	2.93	3.03

conditions; strongly water-wet and strongly oil-wet conditions.

Sintered Bead Pack: Results are given in Fig. 11. The best fit to the water wet drainage data is $n = 2.04$. This is again in excellent agreement with experimental data on sintered glass beads from (Sharma et al., 1990) who reported $\bar{n} = 2.22 \pm .3$. We observe very different n values under oil wet conditions. The oil wet samples exhibit a much higher value of $n > 5$ for all saturations with n increasing with decreasing S_w . This strong difference in n under different wettability conditions mirrors the data of (Sharma et al., 1990); $n = 4.84 \pm 1.6$.

Fontainebleau Sandstone: The simulated data for water wet drainage into the two higher porosity Fontainebleau sandstone samples is given in Fig. 12. In all cases we observe classic Archie behaviour with $n = 2$ for all $S_w \gtrsim 0.15$. At lower saturations the value of n is observed to increase. We observe very different n values under oil wet conditions. The oil wet samples exhibit a much higher value of $n > 5$ for all saturations with n increasing with decreasing S_w . This strong difference in n under different wettability conditions mirrors the data of (Sweeney and Jennings, 1960).

Experimental porous plate RI measurements have been undertaken on a directly adjacent sister plug of the second Fontainebleau sample. This data is shown in Fig. 13.

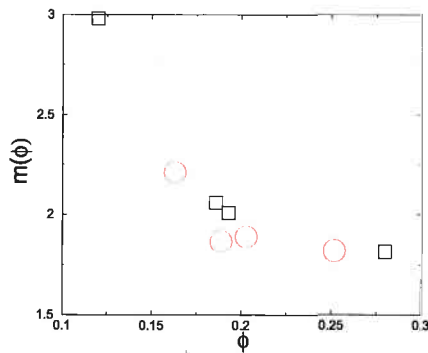


Figure 10: Archie's cementation exponent as a function of ϕ for the four sucrosic samples.

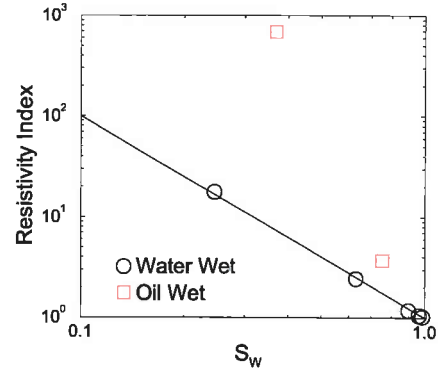


Figure 11: RI vs. S_w plot for the monodisperse bead pack. The solid line shows the trend for $n=2.0$.

The agreement between experiment and simulation for $S_w > .2$ is excellent. The experimental data also exhibits a departure from the classic $n = 2$ behaviour at $S_w < 0.15$, but in the experimental data the value of n decreases at lower water saturations. The reason for the deviation between the experimental and numerical data for low S_w is believed to be due to finite resolution of the image data. At low S_w the water films in the image data become isolated and therefore do not contribute to the overall conductivity of the sample; recall Fig. 7(b) where $S_w \simeq S_{wi}$. In reality, films remain connected by surface roughness on length scales below the resolution of the μ CT. This leads to lower experimental values of n than numerically predicted at low S_w .

Imbibition: Imbibition RI is simulated via film thickening and compared to experiments undertaken via an air/brine porous plate technique on the $\phi = 13\%$ sample. We observe a good match to the resistivity index hysteresis behaviour observed experimentally for $S_w > 20\%$ (Fig. 13). The imbibition RI exhibits $n = 1.5$ in contrast to $n = 2$ for the drainage RI cycle.

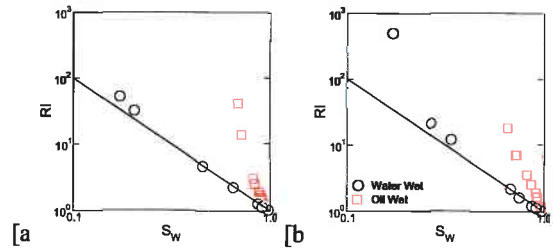


Figure 12: RI vs. S_w plot for the two Fontainebleau samples. Data for the 17% porosity sample is shown in (a) and the 13% porosity sample in (b).

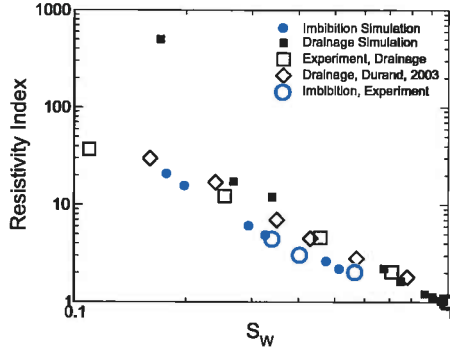


Figure 13: RI vs. S_w plot for drainage and imbibition cycles on Fontainebleau sandstone. Resistivity index hysteresis is observed in good agreement with experiment for $S_w > 20\%$.

Sucrosic Dolomites: We show the data for all sucrosic dolomite samples in Fig. 14. We observe very different n values under water and oil wet conditions. Both samples exhibit non-standard behaviour in the drainage RI curves with S_w . The water wet curves show distinct curvature and n increasing with decreasing S_w . At very low saturations the values of n are consistently less than the default value of $n = 2$, increasing to $n > 2$ at lower saturations. The oil wet samples exhibit a much higher value of $n > 5$ for all saturations and n increasing with decreasing S_w in agreement with (Sweeney and Jennings, 1960).

Anisotropic Sample

Here we consider the resistivity of the sample shown in Fig. 3. We define the z-direction as perpendicular to the bedding planes and x,y axes as parallel to the bedding. Simulation of water saturated resistivity leads to a small resistivity anisotropy in the cementation exponent; $m_x = 1.77$, $m_y = 1.77$ and $m_z = 1.96$.

We then consider the saturation exponent of the clean laminated sample. Very strong anisotropy is observed in Fig. 15. Under water wet conditions we observe $n_{par}^{WW} \simeq 2.7$ parallel to the bedding plane and $n_{perp}^{WW} \simeq 5$ perpendicular to the bedding plane. The data for n_{perp} exhibits strong non-linear trends. Parallel to the bedding plane the saturation exponent under oil wet conditions $n_{par}^{OW} \simeq 3$; a low value for n under oil wet conditions and very similar to the value obtained for water wet conditions. The value perpendicular to the bedding plane under oil-wet conditions exhibits very large values of $n_{perp}^{OW} \simeq 10$.

The similar values of n_{par} under oil-wet and water-wet conditions may be understood by visualising the phase distribution within the image data. An example of the phase distributions within the sample in 2D at $S_w = 0.59$

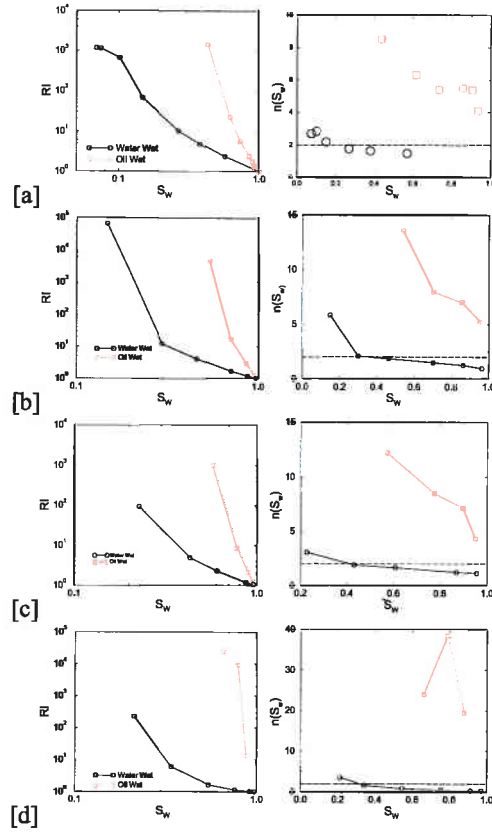


Figure 14: (a-d) Simulation of the resistivity index of sucrosic samples 1-4 respectively. The circles give the data for the water wet conditions and the red squares the data for the oil wet conditions. (Left) gives the original curve and (right) gives the effective value of n for the different wettability conditions as function of S_w .

and $S_w = 0.42$ is shown in Fig. 16. The pores in the tighter laminations remain largely fully water saturated, while the wetting fluid saturation in the coarser grained regions exhibit low water saturations with most of the water present as films. In Fig. 17 we illustrate the network structure of the connected non-wetting phase at the same saturations; $S_w = 0.42$ and 0.59 . In both cases the non-wetting phase remains strongly connected along the bedding plane with the phase concentrated in the coarser laminations. This strong partitioning of the wetting and non-wetting phases leads to the laminations behaving independently (parallel resistors) and therefore similar values being observed under oil-wet and water-wet conditions. The laminations also lead to the clear difference in the resistivity index parallel to the laminations RI_x, RI_y compared to RI perpendicular to the bedding planes RI_z .

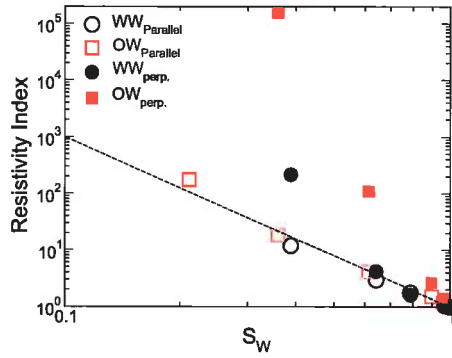


Figure 15: RI vs. S_w plot for laminated sand. The line shows $n = 3$.

Dual Porosity Sample

Simulation of water saturated resistivity was undertaken on a 1200^3 volume. We observe no anisotropy and a consistent value of $m = 1.75$ along all three directions. The RI data is summarized in Fig. 18. We first compare the water wet drainage simulation data (squares) to experiment on sister core material. We note that the simulation gives a slightly smaller value of n ; the variation may be due to heterogeneity in the sample. Imbibition RI simulations exhibits a small degree of hysteresis. Simulation of oil wet drainage exhibits large values of n as was observed in the clastic samples. Overall this idealized dual porosity sample behaves like an Archie rock despite the multimodal pore size distribution.

Complex Bioclastic Samples

Formation Factor Cementation Exponent m

Simulations are performed on a significant subset of the full image volume (1200^3) along three orthogonal axes. For sample 1 we observe variation in the value of Archie's exponent with $m_x = 2.29$, $m_y = 2.31$ and $m_z = 2.45$ with a mean value $\bar{m} = 2.32$. For sample 2 we observe stronger variation in the value of Archie's exponent with orientation ($m_x = 2.34$, $m_y = 2.61$ and $m_z = 2.11$) and $\bar{m} = 2.35$.

The value of the cementation exponent of carbonate rocks has been related (Lucia, 1983) to the amount of interparticle porosity, the amount of separate vug porosity and the presence or absence of touching vugs (see Fig. 7 of (Lucia, 1983)). Lucia argued that the addition of separate vugs to a nonvuggy rock increases porosity but contributes little to the electrical and fluid transport properties of the rock. From the 3D microtomogram (recall Fig. 6) we have already partitioned the macropores into two classes; the connected macropores which are connected globally via a macropore network and the sepa-

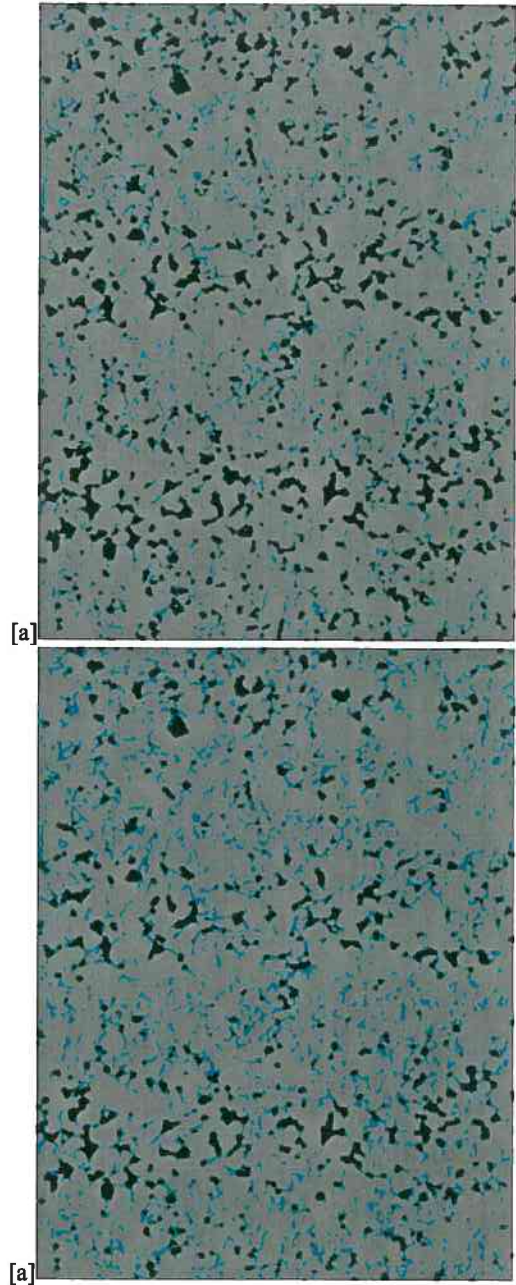


Figure 16: (a) 2D slice of clean laminated sand with wetting phase distribution (blue) and non-wetting phase (black) at $S_w = 0.42$. (b) gives the phase distribution at $S_w = 0.59$.

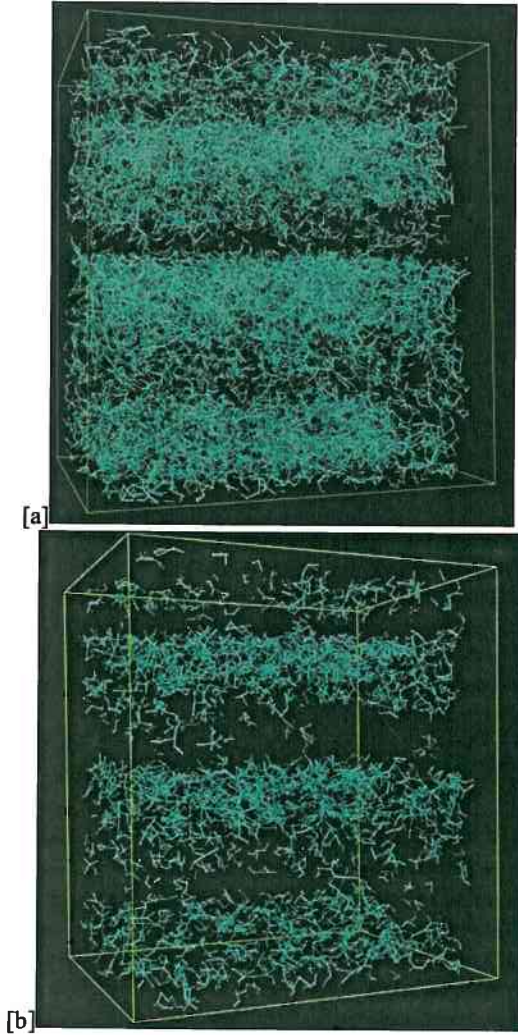


Figure 17: (a) 3D phase distribution of the non-wetting phase at $S_w = 0.42$; (b) shows the same network at $S_w = 0.59$. The partitioning of the non-wetting phase into laminations is evident.

rate macroporosity which are connected only through the meso / micropores (non-resolved pores). In sample 1 we observe 8.2% separate macroporosity in a total porosity of 27.2%. This equates to 30% separate macroporosity and, according to Lucia, an expected exponent $m \simeq 2.3$. In sample 2 we observe 9% separate or isolated macroporosity in a total porosity of 23.2%. This equates to 38% separate macroporosity and accordingly an exponent $m \simeq 2.38$. These results compare very well with the result obtained from the microtomographic images $\bar{m} = 2.32$ and $\bar{m} = 2.35$ respectively.

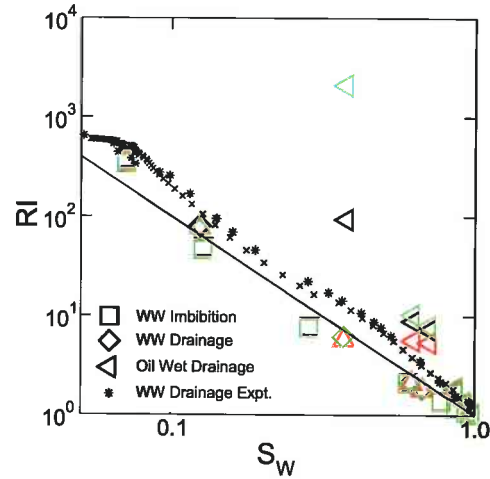


Figure 18: RI under different wettability conditions for the dual porosity sample. The image based data for water wet drainage (squares) can be compared with experimental data performed on a sister core (Padhy et al., 2006) (crosses). The three colours are associated with numerical data simulated along three orthogonal directions on the image sample. No anisotropy is observed.

Saturation Exponent n

Due to the presence of microporosity in these samples the simulations are carried out under slightly different wettability scenarios; mixed-wet and water-wet. Mixed wet conditions attempt to mimic conditions equivalent to experimental laboratory tests for n in restored state core samples. Pores with the *largest* pore throats are assumed to be oil wet and pores with small pores/throats within the unresolved phase remain water wet. In reality the pore throat size at which throats transit from oil wet to water wet depends on the local capillary pressure or the height above the free water level. In the simulation we assume all *resolvable macropores* ($r_t > 3\mu m$) are oil wet and all micropores ($r_t < 3\mu m$) remain water wet. A drainage simulation is then undertaken by oil invasion into the smallest macropores and progressively invading larger pores in the system. The water phase in the larger pores is not trapped as water can drain from the larger pores via water films in the microporosity which is known to be well connected (recall Fig. 6) (Sok et al., 2007). The resultant RI curve is shown in Fig. 19(a) and values of $n(S_w)$ given in Fig. 19(b). We note non-standard behaviour in the drainage RI curves with S_w . The curves show distinct curvature and n exhibiting a maximum value at intermediate S_w and then decreasing with decreasing S_w (black curves). The values of n are consistently less than the default value of $n = 2$ in the drainage cycle and *much lower* than observed in simple samples (1-10) for drainage under oil wet condi-

tions. The reason for the small value of n and the curvature in the RI curve is presumably due to the continuity of the water saturated meso / microporosity. The continuous water saturated meso / microporosity acts as a *parallel pathway* for the electrical current and therefore exhibits lower resistivity (Griffiths et al., 2006) than the other samples considered. One can also simulate wettability conditions associated with oil accumulation. As noted by (Marzouk et al., 1995), original oil accumulation is a true drainage process into a fully water wet rock. We undertake simulations assuming initial water wet conditions in the macropores and find the values of n are extremely low (Fig. 19, red curves). These results are consistent with experimental data previously presented on similar cores from Abu Dhabi (Marzouk et al., 1995) and are again presumably associated with the water saturated microporosity.

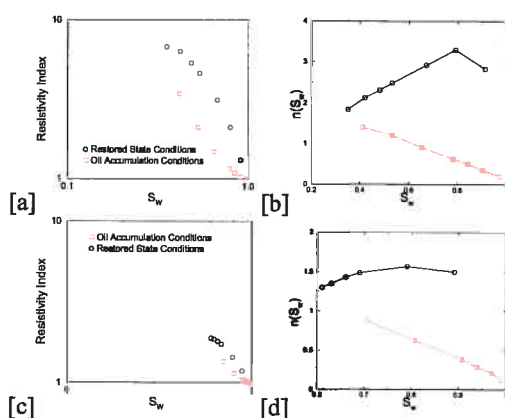


Figure 19: (a,c) Drainage RI for sample 7 under oil- and water-wet conditions in the macroporosity with all microporosity remaining water wet. (b,d) Simulation results for Sample 9; Effective value of n for different wettability conditions as function of S_w .

DISCUSSION

Empirical models used in the interpretation of resistivity logs are not explicit in their predictions of electrical conductivity with respect to rock and pore structure, spatial distribution of fluids, wettability or clay mineral distributions. The evolving development of digital imaging technology and petrophysical analysis on digital image data have potential implications to aid petrophysical interpretations in the future.

Archie vs. Non-Archie samples: Archie's equations are widely used to describe the electrical conductivity of clay free rocks. In this paper we have focused on samples where deviations from Archie's equations occur in clay mineral-free samples. There is an extensive literature

showing the effect of hydrated clay minerals and water salinity on the electrical conductivity of shaly siliclastic rocks. Clay distributions can be imaged via 3D micro-CT technology (see Fig. 20) and the conductivities associated with hydrated clay minerals for shaly granular rocks may be incorporated into the image based calculations (Jin et al., 2007). This will be considered in future work.

Rock Typing: Correlations for petrophysical parameters and saturation dependent transport properties are often grouped by rock type. This is a broad classification including quantitative measures such as porosity, permeability, pore and throat size distributions, pore connectivity and qualitative descriptions of rock fabric and texture. Rock-typing is also based on conventional core analysis data (porosimetry, permeametry, MICP), SCAL, wireline logs (electrofacies), description of cuttings and depositional environment and thin-section analysis. The broad nature of this classification has obvious limitations and fails to fully capture the complex dependence between pore space geometry and topology (rock micro-structure) and petrophysical properties. In this paper we show, for the first time, the potential of 3D imaging to provide correlations between pore structure and resistivity measurements for actual rocks. A comprehensive classification for rocks based on pore scale 3D image data may lead to the establishment of more direct relationships between rock micro-structure and petrophysical properties.

Wettability is arguably the major factor controlling the distribution and flow of fluids in porous rocks and therefore on ultimate recovery of hydrocarbons. In this paper we have considered very primitive wetting scenarios (strongly oil or water wet). These are useful in establishing bounds on the effects of wettability on saturations and recovery, however, they fail to capture the true complexity of wettability distributions in reservoir rocks. In future work we aim to investigate the complex interaction between displacement rate, contact angle and realistic wettability distributions on the RI and relative permeability.

CONCLUSIONS

A 3D imaging and resistivity study has been undertaken on a range of core material from simply sintered bead packs through to complex microporous carbonates.

- **High quality 3D image data** was obtained for the core samples studied. Images comprising 2000^3 voxels were captured at a voxel size of 2.5-8 μm voxel size. Agreement with experimental MICP data was obtained on the image data.
- **Archie's cementation exponent m** from image data is in good agreement with experiment. Data for the sintered bead pack, the Fontainebleau sands

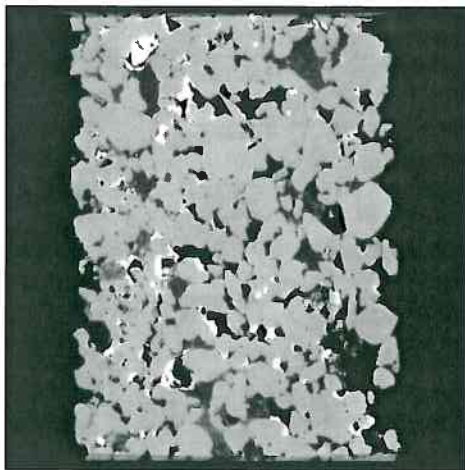


Figure 20: Grey scale tomographic images of clay bearing sand. Siliclastic grains, clean pores and clay filled regions are evident.

and sucrosic dolomites agree well with experiment over a range of ϕ . We do note a consistent increase in the cementation exponent with decreasing porosity. Simple sintered systems ($\phi = 38\%$) give $m < 1.4$, Fontainebleau sands at 13 – 17% give $m = 1.8$ and lower porosity samples $m = 2.2$. This range of m was reported by (Carothers, 1968). We also note an increase in the cementation exponent for the sucrosic dolomite samples with decreasing porosity in agreement with experiment (Fig. 10). The laminated sand sample exhibits only small anisotropy with $m_{par} = 1.77$ and $m_{perp} = 1.96$. The value of the cementation exponent of carbonates may be empirically related to the fraction of disconnected macroporosity as described by Lucia (Lucia, 1983).

- **Drainage RI simulations** were undertaken on the sample data. The prediction of the saturation exponent of the Archie-type rocks from image data is in reasonable agreement with experiment where available. Deviations are observed at low water saturation; this is believed to be due to finite image resolution. Under water-wet conditions the drainage RI for simple clastic rocks considered here do exhibit the predicted Archie-type behaviour— $n = 2$ and constant $n(S_w)$ for $S_w < 0.15$. The simple sucrosic carbonates do exhibit a small but consistent increase in $n(S_w)$ with decreasing S_w . The behaviour of $n(S_w)$ under oil-wet drainage conditions exhibits significantly larger values of the saturation exponent $n > 4 - 5$. The laminated system exhibits strong anisotropy correlated to the bedding axes, but little difference between

oil-wet and water-wet n parallel to the laminations. The dual phase system exhibits classical Archie behaviour and conventional m and n despite the complex pore space. The bioclastic sample exhibit values of n that vary strongly with water saturation. Larger values of n are observed at high S_w , but n decreases markedly with decreasing S_w . These results are consistent with experimental data previously presented on similar cores (Marzouk et al., 1995).

- **Pore and fluid phase connectivity** was illustrated for the image data and can help to explain the resistivity of the rock samples considered here. For example, the reason for the much higher value of the saturation exponent under oil wet conditions for most samples can be easily understood from consideration of the connectivity of the water phase under the two different saturation conditions (recall Fig. 7(a)). This figure shows a phase distribution map of the wetting phase (blue) and the non-wetting phase (black) within the pore space at roughly equivalent fluid phase saturations. It is clear from the figure that the wetting phase is very well connected throughout the pore space and therefore the conductivity of the sample would be rather high (low RI). In contrast, under oil-wet conditions the black phase would indicate where the water would accumulate; under these conditions the water is more poorly connected and exhibits much lower conductivity (higher RI). The continuity of the wetting/non-wetting phase in the laminated sample leads to the resultant anisotropy in n . The values of n observed for the complex carbonates are, based on conventional thinking, very low for a system exhibiting oil wet conditions. The reason for the small value of n is associated with the continuity of the water saturated meso / microporosity which is directly imaged. The continuous water saturated microporosity acts as a parallel path for the electrical current leading to lower n values at low S_w .

ACKNOWLEDGEMENTS

The authors acknowledge the Australian Research Council and the member companies of the Digital Core Consortium for their support. We thank Total and Japan Oil Gas and Metals Corporation for permission to present some of the data in this work. We thank the A.N.U. Supercomputing Facility and the Australian Partnership for Advanced Computing for very generous allocations of computer time.

REFERENCES CITED

- Arns, C. H., Knackstedt, M. A., Pinczewski, W. V., and Lindquist, W. B., 2001, Accurate computation of transport properties from microtomographic images: *Geophysical Research Letters*, **28**, 3361–3364.
- Arns, C. H., Knackstedt, M. A., Pinczewski, W. V., and Garboczi, E. G., 2002, Computation of linear elastic properties from microtomographic images: Methodology and agreement between theory and experiment: *Geophysics*, **67**, no. 5, 1396–1405.
- Arns, C. H., Knackstedt, M. A., Pinczewski, W. V., and Martys, N., 2004, Virtual permeametry on microtomographic images: *J. Petroleum Sci. and Eng.*, **45**, 41–46.
- Arns, C. H., Baugé, F., Limaye, A., Sakellariou, A., Senden, T. J., Sheppard, A. P., Sok, R. M., Pinczewski, W. V., Bakke, S., Berge, L. I., Oren, P. E., and Knackstedt, M. A., December 2005, Pore scale characterization of carbonates using micro x-ray ct: *SPE Journal*, pages 475–484.
- 2005b, Digital core laboratory: Petrophysical analysis from 3d images: *Petrophysics*, **46** (4), 260–277.
- Bohn, R. B., and Garboczi, E. J., User manual for finite element and finite difference programs: A parallel version of NISTIR-6269; Technical report, NIST Internal Report 6997, 2003.
- Carothers, J. E., 1968, A statistical study of the formation factor relation: *The Log Analyst*, **9**, 13–20.
- Doyen, P., 1988, Permeability, conductivity and pore geometry of sandstone: *J. Geophys. Res.*, **93**, 7729–7740.
- Fleury, M., Efnik, M., and Kalam, M. Z., October 2004, Evaluation of water saturation from resistivity in a carbonate field. from laboratory to logs; SCA2004–22.
- Focke, J. W., and Munn, D., 1987, Cementation exponents in middle eastern carbonate reservoirs: *SPE Formation Evaluation*, **2**, 155–167.
- Garboczi, E. J., and Day, A. R., 1995, An algorithm for computing the effective linear elastic properties of heterogeneous materials: three-dimensional results for composites with equal phase Poisson ratios: *J. Mech. Phys. Solids*, **43**, no. 9, 1349–1362.
- Griffiths, R., Carnegie, A., Gyllensten, A., Ribeiro, M., Prasodjo, A., and Sallam, Y., 2006, Evaluation of low resistivity pay in carbonates; a breakthrough; Presented at the SPWLA Annual Logging Symposium.
- Jacquín, C. G., 1964, Corrélation entre la perméabilité et les caractéristiques géométriques du grès de fontainebleau: *Revue Inst. fr. Pétrole*, **19**, 921.
- Jin, G., Torres-Verdin, C., Devarajan, S., Toumelin, E., and Thomas, E. C., 2007, Pore scale analysis of the waxman-smits shaly-sand conductivity model: *Petrophysics*, **48** (2), 104–120.
- Knackstedt, M. A., Arns, C. H., Sakellariou, A., Senden, T. J., Sheppard, A. P., Sok, R. M., Pinczewski, W. V., and Bunn, G. F., 2004, Digital core laboratory: Properties of reservoir core derived from 3d images; Presented at the Asia-Pacific Conference on Integrated Modelling for Asset Management, SPE 87009.
- Lucia, F., March 1983, Petrophysical parameters estimated from visual descriptions of carbonate rocks: A field classification of carbonate pore space: *Journal of Petroleum Technology*, **35**, 629–637.
- Marzouk, I., Takezaki, H., and Miwa, M., 1995, Geologic controls on wettability of carbonate reservoirs: Geologic controls on wettability of carbonate reservoirs; Society of Petroleum Engineers.
- Padhy, G. S., Ioannidis, M. A., Lemaire, C., and Coniglio, M., September 2006, Measurement and interpretation of non-archie resistivity behavior in model and real vuggy carbonates: SCA 2006: Improved Core Analysis driven by Field Development Needs, SCA2006–11.
- Sakellariou, A., Sawkins, T. J., Senden, T. J., and Limaye, A., 2004a, X-ray tomography for mesoscale physics applications: *Physica A*, **339**, 152–158.
- 2004b, An x-ray tomography facility for a wide range of mesoscale physics applications, SPIE, Proceedings of SPIE, 166–171.
- Sharma, M. M., Garrouch, A., and Dunlap, H. F., 1990, Effect of wettability, pore geometry and stress on electrical conduction in fluid-saturated rocks: *The Log Analyst*, **32**, 511–526.
- Sok, R. M., Arns, C. H., Knackstedt, M. A., Sheppard, A. P., Senden, T. J., Pinczewski, W. V., and Okabe, H., 2007, Estimation of petrophysical parameters from 3d images of carbonate core; Presented at the SPWLA Middle East Regional Symposium.
- Sweeney, S. A., and Jennings, H. Y., 1960, Effect of wettability on the electrical resistivity of carbonate rock from a petroleum reservoir: *J. Phys. Chem.*, **64**, 551–553.

Toumelin, E., Torres-Verdin, C., Davarajan, S., and Sun, B., September 2006, An integrated pore scale approach for the simulation of grain morphology, wettability and saturation history effects on electrical resistivity and nmr measurements of saturated rocks; SCA2006-20.

Wong, P., Koplik, J., and Tomanic, J. P., 1984, Conductivity and permeability of rocks: Phys. Rev. B, 30, no. 11, 6606-6614.

Worthington, P. F., and Pallatt, N., 1992, Effect of variable saturation exponent on the evaluation of hydrocarbon saturation: SPE Form. Eval., pages 331-336.

Worthington, P. F., 2005, An electrical analog facility for hydrocarbon reservoirs: An electrical analog facility for hydrocarbon reservoirs; Presented at the SPE Annual Technical Conference, SPE96718.

ABOUT THE AUTHORS

M.A. Knackstedt: Mark Knackstedt was awarded a BSc in 1985 from Columbia University and a PhD in Chemical Engineering from Rice University in 1990. He is Professor and Head of the Department of Applied Mathematics at the Australian National University and a Visiting Professor at the School of Petroleum Engineering at the University of NSW. His primary interests lie in modelling transport, elastic and multi-phase flow properties of geological materials and development of 3D tomographic image analysis for complex materials.

C. H. Arns: Christoph Arns was awarded a Diploma in Physics (1996) from the University of Technology Aachen and a PhD in Petroleum Engineering from the University of New South Wales in 2002. He is a Senior Research Fellow at the Department of Applied Mathematics at the Australian National University. His research interests include the morphological analysis of porous complex media from 3D images and numerical calculation of transport and linear elastic properties with a current focus on NMR responses and dispersive flow.

A.P. Sheppard: Adrian Sheppard received his B.Sc. from the University of Adelaide in 1992 and his PhD in 1996 from the Australian National University and is currently a Research Fellow in the Department of Applied Mathematics at the Australian National University. His research interests are network modelling of multiphase fluid flow in porous material, topological analysis of complex structures, and tomographic image processing.

T.J. Senden: Timothy John Senden received his training and PhD in physical chemistry at the Australian National University in 1994. His principal techniques are

atomic force microscopy and surface force measurement, but more recently micro-X-ray tomography. His research centres around the application of interfacial science to problems in porous media, granular materials, polymer adsorption and single molecule interactions.

R. M. Sok: Rob Sok studied chemistry and received his PhD (1994) at the University of Groningen in the Netherlands and is currently a Research Fellow in the Department of Applied Mathematics at the Australian National University. His main areas of interest are computational chemistry and structural analysis of porous materials.

Y. Cinar: Yildiray Cinar holds BS and MS degrees from Istanbul Technical Univ. and a PhD from Clausthal Tech. Univ. all in Petroleum Engineering. Prior to joining the School of Petroleum Engineering at UNSW he was a research associate at Stanford Univ. working with Prof. Lynn Orr in the area of multiphase flow in porous media.

W. V. Pinczewski: W.V Pinczewski holds BE (Chem.Eng) and PhD degrees from the University of New South Wales (UNSW). He is Professor and Head of the School of Petroleum Engineering at UNSW. His research interests include improved oil recovery, multi-phase flow and transport properties in porous media and network modelling.

Marios Ioannidis received a Dipl. Eng. from the University of Patras, Greece, in 1989, and a Ph.D. Degree from the University of Waterloo, Canada, in 1993, both in Chemical Engineering. He is Associate Professor at the Department of Chemical Engineering, University of Waterloo, and Director of the Nanotechnology Engineering Program. His main research interests include pore structure characterization, multiphase flow, solute transport and magnetic resonance in porous media, with applications to hydrocarbon formation evaluation, contaminant hydrogeology and fuel cell engineering.

Girija Padhy has a Masters in Petroleum Technology from University of Pune, India and most recently has been a PhD candidate at the University of Waterloo studying petrophysical characterization of vuggy carbonates. He is now a Senior Petrophysicist for Schlumberger in Kuwait where he works on log interpretation and core-log integration for characterization of vuggy carbonate reservoirs.